

Article

Copper and Iron Cooperation on Micro-Spherical Silica during Methanol Synthesis via CO₂ Hydrogenation

Serena Todaro¹, Francesco Frusteri¹, Dariusz Wawrzyńczak², Izabela Majchrzak-Kuceba², Juan-Francisco Pérez-Robles³, Catia Cannilla¹  and Giuseppe Bonura^{1,*} 

¹ CNR-ITAE, Istituto di Tecnologie Avanzate per l'Energia "Nicola Giordano", Via S. Lucia Sopra Contesse, 5, 98126 Messina, Italy; serena.todaro@itae.cnr.it (S.T.); francesco.frusteri@itae.cnr.it (F.F.); catia.cannilla@itae.cnr.it (C.C.)

² Department of Advanced Energy Technologies, Czestochowa University of Technology, Dabrowskiego 73 St., 42-201 Czestochowa, Poland; dwawrzynczak@is.pcz.pl (D.W.); izak@is.pcz.pl (I.M.-K.)

³ Cinvestav Libramiento, Laboratorio de Materiales Nanoestructurados y Caracterización Electroquímica, Norponiente, #2000, Fracc. Real de Juriquilla, Santiago de Querétaro 76230, Mexico; jfperez@cinvestav.mx

* Correspondence: giuseppe.bonura@itae.cnr.it

Abstract: A series of mono- and bi-metallic copper and iron samples were prepared by impregnation method on micro-spherical silica and used for the synthesis of methanol via CO₂ hydrogenation. Compared with conventional carrier oxides, micro-spherical silica has obvious advantages in terms of absorption capacity and optimal distribution of active phases on its surface, also exhibiting excellent heat resistance properties and chemical stability. The prepared catalysts were characterized by various techniques including XRF, XRD, SEM, TEM, H₂-TPR and CO₂-TPD techniques, while catalytic measurements in CO₂ hydrogenation reaction to methanol were performed in a fixed bed reactor at a reaction pressure of 30 bar and temperature ranging from 200 to 260 °C. The obtained results revealed that the mutual interaction of copper–iron induces promotional effects on the formation of methanol, especially on systems where Fe enrichment on the silica support favours the presence of a larger concentration of oxygen vacancies, consequently responsible for higher CO₂ adsorption and selective methanol production. Surface reconstruction phenomena rather than coke or metal sintering were responsible for the slight loss of activity recorded on the catalyst samples during the initial phase of reaction; however, with no appreciable change on the product selectivity.

Keywords: micro-spherical silica; CO₂ hydrogenation; methanol; Cu catalysts; Fe catalysts



Citation: Todaro, S.; Frusteri, F.; Wawrzyńczak, D.; Majchrzak-Kuceba, I.; Pérez-Robles, J.-F.; Cannilla, C.; Bonura, G. Copper and Iron Cooperation on Micro-Spherical Silica during Methanol Synthesis via CO₂ Hydrogenation. *Catalysts* **2022**, *12*, 603. <https://doi.org/10.3390/catal12060603>

Academic Editors: Consuelo Alvarez-Galvan and Hamidreza Arandiyani

Received: 4 May 2022

Accepted: 31 May 2022

Published: 31 May 2022

Publisher's Note: MDPI stays neutral with regard to jurisdictional claims in published maps and institutional affiliations.



Copyright: © 2022 by the authors. Licensee MDPI, Basel, Switzerland. This article is an open access article distributed under the terms and conditions of the Creative Commons Attribution (CC BY) license (<https://creativecommons.org/licenses/by/4.0/>).

1. Introduction

In the last number years the concentration of carbon dioxide (CO₂) in the atmosphere has greatly increased owing to human activities, in particular from burning fossil fuels for electricity, heat and transportation. The anthropic production of carbon dioxide increases the natural greenhouse effect, considered as the main issue related to climate change and global warming [1–3]. In this regard, many researchers have been focusing on the potential of carbon capture and utilization (CCU) strategies to produce high-added-value compounds such as methanol, dimethyl ether, methane, and other hydrocarbons [4–9], by realizing an ideal neutral carbon-loop when CO₂ is reacted with green hydrogen coming from renewable sources [10–13].

Being considered as one of the most efficient energy carriers in the concept of a new sustainable economy [14–16], methanol (MeOH) is traditionally produced from syngas by catalytic hydrogenation at high temperature and pressure, determining a serious impact on the environment.

So, the potential use of CO₂ as an alternative feedstock replacing syngas in the methanol production has drawn widespread attention as an effective way to recycle carbon and reduce CO₂ emissions [17–21]. CuO/ZnO/Al₂O₃ is a conventional catalyst for

methanol synthesis from syngas and its effectiveness has also been demonstrated in the hydrogenation of CO₂. Unfortunately, CO₂-to-MeOH hydrogenation reaction still faces many problems due to low reactivity and high thermodynamic stability of CO₂, which determines its low conversion [22–25].

Nevertheless, Al₂O₃ has been recognized as a poorly effective carrier oxide for methanol catalyst during CO₂ hydrogenation, due to its strong hydrophilic character. This is because a huge amount of water is formed during the reaction and Al₂O₃ tends to strongly adsorb it on its surface, causing the blocking of the active centres of the catalyst [26]. Really, alternative catalyst compositions, wherein Al₂O₃ was exchanged with ZrO₂, have proven to be more stable under the typical reaction conditions [27–29], but in any case the most adopted catalyst formulations always contain copper as the main component, combined in binary, ternary or in a higher multiplicity with other metal oxides, and even differently promoted [24,25]. Despite this, large efforts have also been devoted to individuate operative conditions and reactor configurations more suitable to address the activity-selectivity pattern; however, the design of novel active phases targeting large scale productivity still represents the main challenge. For this reason, many authors have focused their attention on the peculiarities of metal supported catalysts, in order to isolate specific effects on the catalytic surface (i.e., metallic surface area, metallic dispersion, metal-oxide interface, . . .) from possible contributions of the support. Indeed, iron as a typical active phase for Fischer–Tropsch (FT) synthesis was suggested to improve the inter-dispersion of mixed metal oxides and the interactions between Cu species and other metal oxides during CO or CO₂ hydrogenation reaction [30–32]; additionally inhibiting the sintering and re-oxidation of copper and enhancing the catalytic stability of Cu-based catalysts at high temperatures for the RWGS reaction [33]. However, the use of catalytic formulations based on Cu-Fe for the CO₂ hydrogenation to methanol is rarely reported in literature, despite the fact that they represent potential candidates suitable to deliver high selectivity to alcohols under mild conditions in the presence of syngas as feedstock [34–37]. Moreover, SiO₂ as a support has been widely used in the methanol production but its use in the form of spherical carrier oxide for the CO₂ hydrogenation reaction has been less documented, provided that it possesses well-defined features of morphology, surface area or thermal stability as well as good compatibility with other materials [38,39].

In this work, micro-spherical silica was used as support for either mono-metallic Cu and Fe or bi-metallic Cu-Fe systems at different Cu/Fe atomic ratio, in order to disclose the relationships between structure and catalytic properties during synthesis of methanol via CO₂ hydrogenation. The silica sample was chosen with a micro-spherical morphology due to its capability to probe the intrinsic effects of copper and iron as isolated phases or as a cooperative effect, without bringing any specific catalytic contribution alike to other common carrier oxides, such as ZnO [40–42], Al₂O₃ [43–46] or ZrO₂ [27–29,47,48], typically entering into the formulation of methanol catalysts. At the same time, the micro-spherical features of silica offer an adequate stability and textural properties that allow for an optimal distribution of the active metallic phase on its surface. Despite the well-known behaviour of Cu-ZnO-Al₂O₃ (CZA) or CuO-ZnO-ZrO₂ (CZZ) compositions for the methanol production, the final goal of this work is to highlight how the cooperation between Cu and Fe atoms prompted by interaction on micro-spherical SiO₂ is beneficial for developing catalytic systems with physico-chemical and catalytic properties controlling CO₂ activation and methanol formation.

2. Results and Discussion

The SEM images in Figure 1—left show the morphology of the “bare” ES70Y micro-spherical silica used as support for the metallic phase. In particular, the silica sample appears quite compact, being characterized by a uniform distribution of regular spheres with an average diameter between 40 and 100 μm.

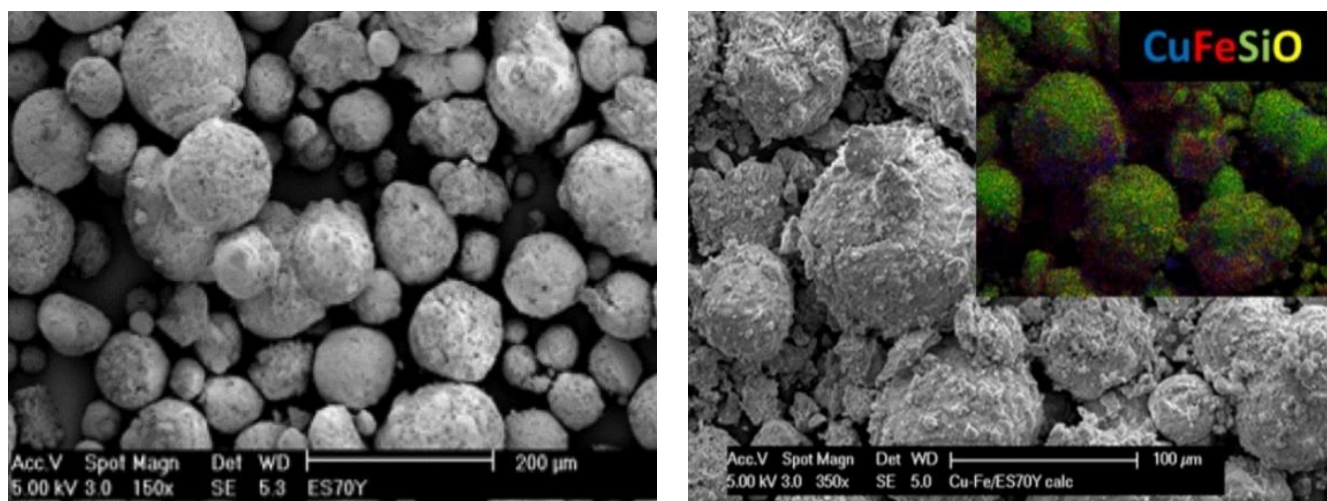


Figure 1. SEM micro-graphs of the “bare” ES70Y micro-spherical silica (**left**) and a representative Cu(x)Fe(y)-Si catalyst sample (**right**). In the inset the elemental mapping of the bimetallic catalyst is represented.

Regarding the supported samples (Figure 1—right), the SEM micro-graph of a representative bimetallic Cu(x)Fe(y)-Si sample shows how the spherical morphology of the silica support is preserved upon metal deposition, while the elemental mapping depicted as the impregnation method does not allow for a perfect homogenization of the bimetallic phase on the support, just exhibiting some patchy metal overloading at the bottom of silica spheres.

The list of the investigated catalysts, the relative Fe/(Cu + Fe) ratio determined from the analytical composition and the main textural properties are reported in Table 1.

Table 1. List of catalysts, analytical composition, and textural properties.

Catalyst Sample	Analytical Comp. (mmol/g _{cat}) ^(a)		Fe/(Cu + Fe) (at/at)	S _{BET} ^(b) (m ² /g)	PV ^(b) (cm ³ /g)
	Cu	Fe			
Cu(3)Fe(7)-Si	1.1	2.2	0.67	226 ± 1.9	2.15
Cu(5)Fe(5)-Si	1.6	1.6	0.50	219 ± 1.6	1.96
Cu(7)Fe(3)-Si	2.1	1.0	0.33	213 ± 2.1	2.27
Cu(10)-Si	1.6	-	0.00	149 ± 1.8	1.71
Fe(10)-Si	-	1.6	1.00	272 ± 2.7	3.17

^(a) From XRF analysis; ^(b) From N₂ ads/des isotherms at −196 °C after sample reduction.

Although the metal addition leads to a slight decrease in the surface area with respect to the bare silica micro-spheres, textural data of the supported catalysts evidence that both total surface exposure and pore volume take advantage from a progressive decrease in Cu loading in the catalyst formulation, with the maximum values, respectively, of 272 m²/g and 3.17 cm³/g found for the copper-free catalyst, Fe(10)-Si. In particular, Figure 2 shows how the surface area linearly increases with the molar fraction of iron, by reaching a value as high as 272 m²/g at the Fe/(Cu + Fe) ratio of 1.00.

The XRD patterns of the bi-metallic Cu(x)Fe(y)-Si samples after calcination and reduction are shown in Figure 3.

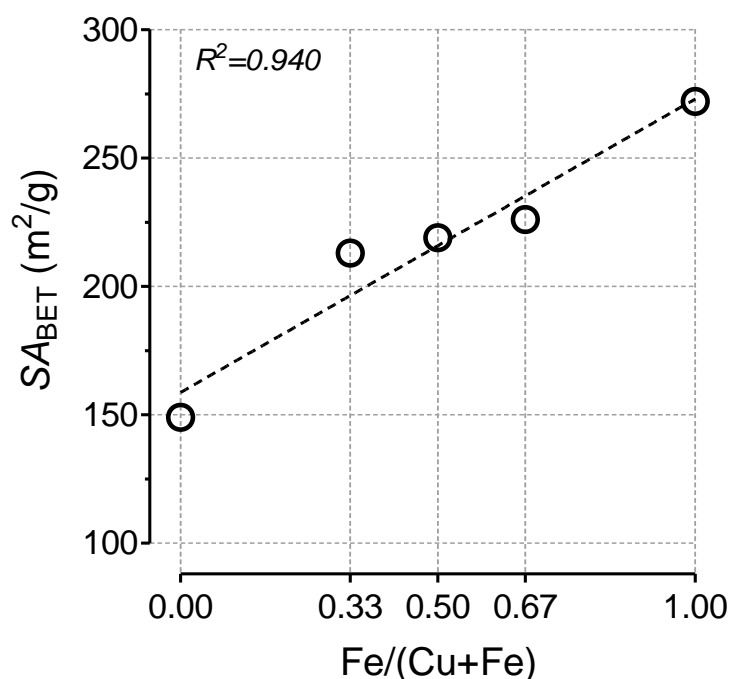


Figure 2. Effect of the Fe/(Cu + Fe) atomic fraction on the surface exposure (S_{BET}).

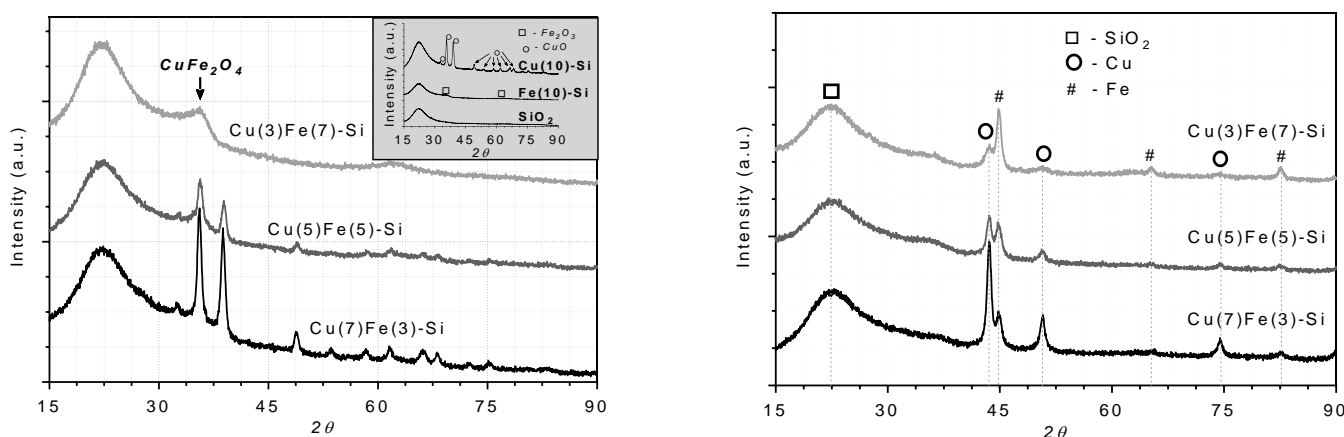


Figure 3. XRD patterns of the Cu(x)Fe(y)-Si catalysts after calcination (left) and reduction (right).

Irrespective of the catalyst state (whether calcined or reduced), a broad band centered at around 22.5° and attributable to amorphous silica is evident for all the samples. In the calcined samples (Figure 3—left), the typical diffraction peaks of CuO well crystallized in the form of tenorite at 35.5 and 38.7° (JCPDS 05-0661) are well visible in the Cu(7)Fe(3)-Si sample, while as the iron loading increases, these reflections tend to decrease in intensity, till the appearance of a mixed oxide form in the Cu(3)Fe(7)-Si sample attributable to the cubic structure of a cuprospinel (CuFe_2O_4 , JCPDS 25-0283). In any case, only low-intensity reflections ascribable to the cubic structure of maghemite (Fe_2O_3 , JCPDS 39-1346) are detected on all the samples, consistent with the fact that Fe ions and Fe nanodomains are evidently embedded into the amorphous background of the SiO_2 phase. After reduction (Figure 3—right), the Cu(x)Fe(y)-Si samples exhibit the formation of the respective metallic phases of copper at 43° (JCPDS 04-0836) and iron at 45° (JCPDS 06-0696), whose relative intensities are proportional to the metal loading on the micro-spherical silica.

In order to determine the redox properties of the catalysts, Figure 4 shows the profiles of the temperature programmed measurements performed under hydrogen atmosphere (H_2 -TPR), while the quantitative results are reported in Table 2.

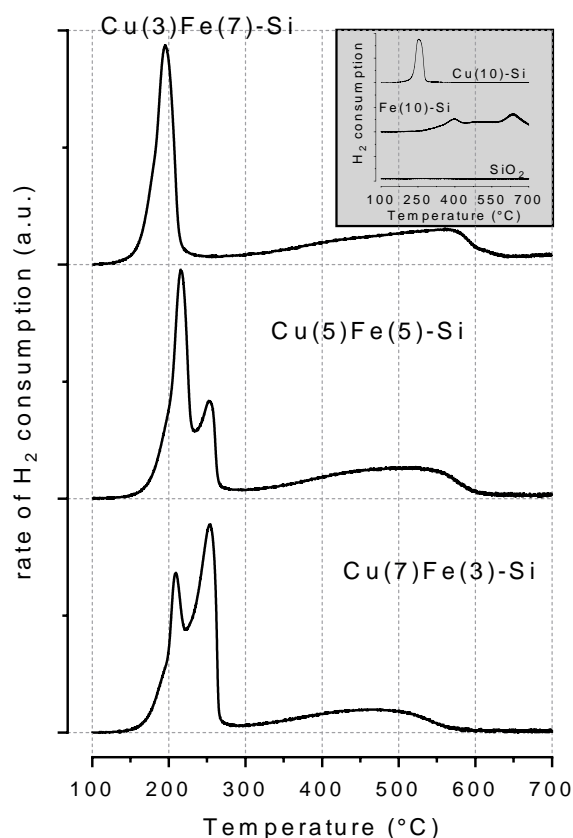


Figure 4. TPR profiles of the bi-metallic Cu(x)Fe(y)-Si catalysts. In the inset, the TPR profiles of the mono-metallic Cu(10)-Si and Fe(10)-Si samples are reported as a reference.

Table 2. Quantitative data from H₂-TPR measurements.

Catalyst Sample	H ₂ Consumption (mmolH ₂ /g _{cat})	T _{0,red} (°C)	T _{max,1} (°C)	T _{max,2} (°C)	α ^(a)
Cu(3)Fe(7)-Si	2.8	208	208	255	0.85
Cu(5)Fe(5)-Si	3.0	120	216	252	0.95
Cu(7)Fe(3)-Si	3.0	108	196	-	0.99
Cu(10)-Si	1.5	151	253	-	0.98
Fe(10)-Si	1.3	238	398	-	0.82

^(a) Fraction of copper and iron oxides reduced to metallic form.

In all the temperature range investigated, the bare SiO₂ sample does not show any baseline drift due to H₂ consumption, while the Cu(10)-Si sample displays a sharp and quite symmetric peak between 170 and 200 °C, mirroring the reduction in CuO to metallic copper. As for the Fe(10)-Si sample, two broad and poorly resolved bands are observed above 300 °C, diagnostic of the progressive reduction in Fe₂O₃ to Fe₃O₄ and then to FeO, before being followed by the reduction to metallic Fe [49].

Regarding the bi-metallic systems, the H₂-TPR measurements are essentially characterized by two convoluted reduction maxima at low ($T_{max,1}$, 196–216 °C) and high temperature ($T_{max,2}$, 252–255 °C), related to the reduction in copper and iron oxide particles, respectively, in less or more synergy among them. In spite of a similar H₂ consumption for all the bi-metallic catalysts (2.8–3.0 mmol/g_{cat}), the molar fraction of iron significantly affects the reduction kinetics in each sample [50], so that in Cu(7)Fe(3)-Si a single peak is observed as the result of easier reduction kinetics ($\alpha = 0.99$) boosted by a low iron enrichment of the sample and exemplified by a shift in the reduction onset temperature (108 °C).

TEM micro-graphs of the calcined and reduced Cu(5)Fe(5)-Si are displayed in Figure 5, showing how the copper and iron phases distribute onto the silica carrier. Despite a not

ideal homogenization of the supported active phase determined by the adopted preparation method, it is evident that the size regularity of silica spheres allows the generation of a metallic phase with homogeneous distribution of particles between 13 and 19 nm.

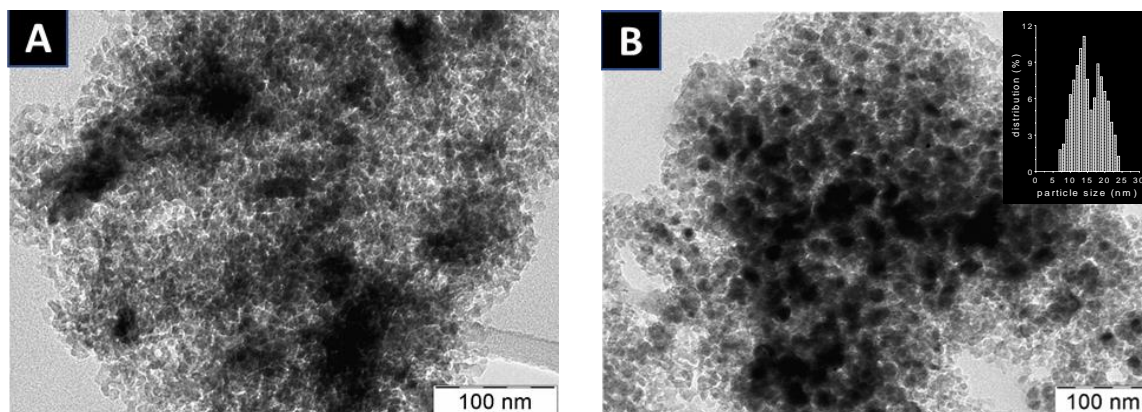


Figure 5. TEM image of the Cu(5)Fe(5)-Si sample: (A) calcined at 500 °C in air; (B) reduced at 400 °C under H₂ atmosphere.

Considering that the catalytic behaviour is primarily controlled by CO₂ activation, CO₂ desorption measurements were performed to determine the relative abundance of the surface adsorption sites on the various investigated catalysts, with profiles and quantitative data reported in Figure 6 and Table 3, respectively.

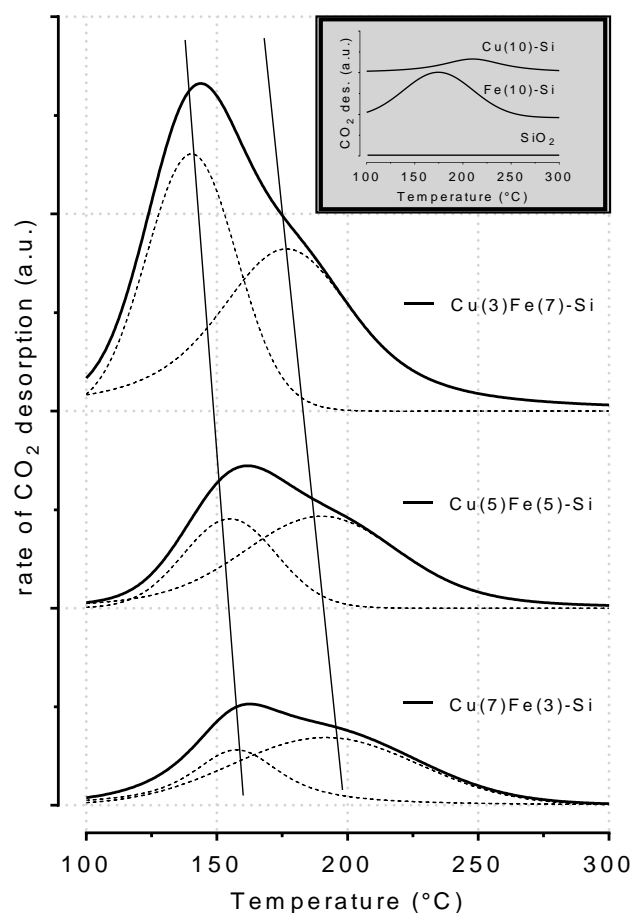


Figure 6. CO₂-TPD profiles of the Cu(x)Fe(y)-Si catalysts. In the inset, the TPD profiles of the bare SiO₂ sample along with mono-metallic Cu/SiO₂ and Fe/SiO₂ samples are reported.

Table 3. Surface properties of the investigated catalyst samples from CO₂-TPD measurements.

Catalyst Sample	$\mu\text{mol/g}_{\text{cat}}$	CO ₂ Uptake	
		n_1 ^(a)	n_2 ^(b)
Cu(3)Fe(7)-Si	50	0.56	0.44
Cu(5)Fe(5)-Si	39	0.48	0.52
Cu(7)Fe(3)-Si	24	0.31	0.69
Cu(10)-Si	5	-	1.00
Fe(10)-Si	28	0.08	0.92
SiO ₂	2	1.00	-

^(a) Population fraction of weak–medium CO₂ sites in the T range < 175 °C. ^(b) Population fraction of strong CO₂ sites in the T range > 175 °C.

So, despite an irrelevant CO₂ coverage on the bare SiO₂ (2 $\mu\text{mol/g}_{\text{cat}}$), it can be observed that for all the bi-metallic Cu(x)Fe(y)-Si samples, the CO₂ uptake concentrates on the temperature range between 100 and 300 °C, as the result of similar convoluted desorption bands, more or less shouldered on the high-temperature side and associated with two main CO₂ populations of weak–medium (below 175 °C) or medium–strong sites (above 175 °C), respectively. In particular, in line with the desorption patterns of the mono-metallic Cu(10)-Si and Fe(10)-Si catalysts, in the bi-metallic samples, not only the CO₂ capacity increases with the iron loading but also the temperature of desorption maxima shift at a lower temperature, so that on Cu(3)Fe(7)-Si the CO₂ uptake as high as 50 $\mu\text{mol/g}_{\text{cat}}$ is mainly to put in relation to the largest population of weak–medium sites (0.56) associated with surface hydroxyl groups or metal-oxygen pairs [51], while on Cu(7)Fe(3)-Si (24 $\mu\text{mol}_{\text{CO}_2}/\text{g}_{\text{cat}}$), a prevailing concentration of medium–strong sites (0.69) is diagnostic of oxygen vacancies generated on the catalyst surface [52,53].

To verify and quantify the possible generation of oxygen vacancies directly linked to the CO₂ adsorption capacity brought by the iron enrichment, in Figure 7 the XPS analysis performed over the bimetallic reduced samples is displayed. The survey scans show the presence of copper in the metallic state at 932.9 eV (Cu 2p_{3/2}), while iron is present at Fe(III), Fe(II) and Fe(0) oxidation states as evidenced by complex multiplet-split Fe 2p spectra at 710.9, 709.6 and 706.6 eV, respectively, with their typical satellite features (Fe and Cu multiplex peak data reported in the Supplementary Material Figure S1a,b). In quantitative terms, all the samples exhibit a surface enrichment of iron over the surface, considering that the Fe/(Cu + Fe) surface ratio is always greater (0.85 for Cu(3)Fe(7)-Si, 0.62 for Cu(5)Fe(5)-Si and 0.54 for Cu(7)Fe(3)-Si) than the respective bulk composition (see Table 1). The O 1s core level spectra were deconvoluted according to three main peaks, associated with lattice oxygen of metal oxides (O_L), oxygen vacancies (O_V) and chemisorbed oxygen on the surface (O_C) from low to high binding energies [54]. The relative concentrations of oxygen species were reported in Table 4 through quantitative analysis based on peak area.

Table 4. Relative concentration of oxygen species calculated from the O 1s peak area.

	Cu(7)Fe(3)-Si			Cu(5)Fe(5)-Si			Cu(3)Fe(7)-Si		
	O_L	O_V	O_C	O_L	O_V	O_C	O_L	O_V	O_C
BE (eV)	532.9	534.7	-	532.8	534.9	535.9	532.8	534.8	535.9
%	96	4	-	84	9	7	72	24	4

As a rule, the percentage of oxygen vacancies generated over the samples linearly increases with the iron loading, from a minimum value of 4% over the Cu-rich sample until a maximum of 24% over the Cu(3)Fe(7)-Si sample at higher Fe loading, in a strong consistency with the previously reported results. Being offset by a decrease in lattice oxygen, these findings clearly suggest that the generation of oxygen vacancies upon the reducing treatment also proceeds according to a mechanism of migration of oxygen species from inside the bulk to the catalyst surface [54,55].

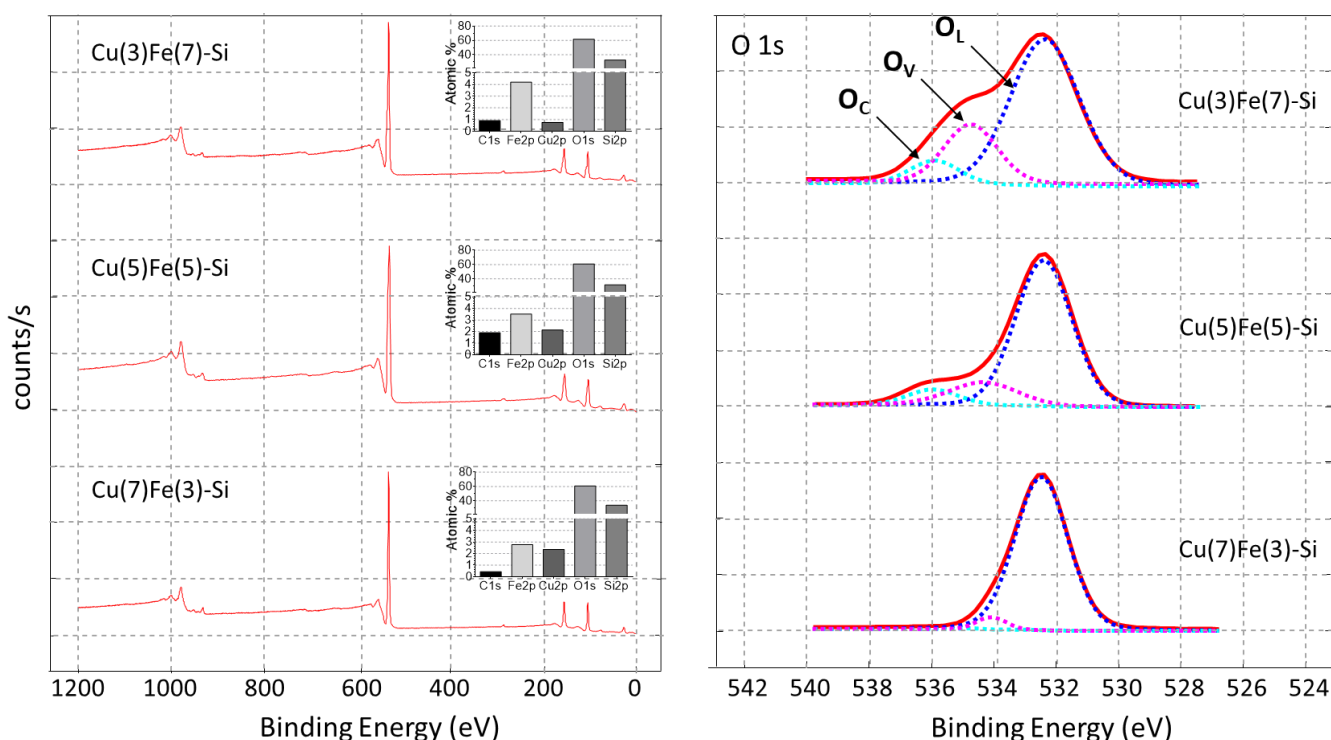


Figure 7. XPS survey scans of the reduced bimetallic samples (left) and deconvolution of O 1s peak (right).

The catalytic behaviour of the prepared samples was investigated under CO₂ hydrogenation conditions and in Table 5 the results obtained at 30 bar in the temperature range of 200–260 °C are reported, in terms of carbon dioxide conversion and product selectivity. As a rule, for all the samples a progressive increase in the CO₂ conversion is recorded with temperature, while methanol selectivity exhibits a clear drop, offset by a regular rise in CO and CH₄ selectivity, in line with thermodynamic predictions [26]. In particular, by inspecting the activity-selectivity pattern of the mono-metallic systems, a superior functionality is observed over the Fe(10)-Si sample, with a maximum CO₂ conversion of 4.6% attained at 260 °C, resulting in MeOH, CO and CH₄ selectivity of 18.0, 54.6 and 27.4%, respectively.

Table 5. Conversion/selectivity data ($X_{\text{CO}_2}/S_{\text{MeOH}}/S_{\text{CO}}/S_{\text{CH}_4}$) in the CO₂ hydrogenation reaction at different temperatures (P_R , 30 bar; GHSV: 8800 NL/kg_{cat}/h).

Catalyst Sample	T_R , 200 °C	T_R , 220 °C	T_R , 240 °C	T_R , 260 °C
	$X_{\text{CO}_2}/S_{\text{MeOH}}/S_{\text{CO}}/S_{\text{CH}_4}$ (%)	$X_{\text{CO}_2}/S_{\text{MeOH}}/S_{\text{CO}}/S_{\text{CH}_4}$ (%)	$X_{\text{CO}_2}/S_{\text{MeOH}}/S_{\text{CO}}/S_{\text{CH}_4}$ (%)	$X_{\text{CO}_2}/S_{\text{MeOH}}/S_{\text{CO}}/S_{\text{CH}_4}$ (%)
Cu(3)Fe(7)-Si	2.4/64.9/30.5/4.6	4.3/55.6/40.2/4.2	7.4/47.6/48.4/4.0	11.6/35.4/57.6/7.0
Cu(5)Fe(5)-Si	2.7/65.5/34.5/0.0	3.8/57.8/42.2/0.0	6.3/46.7/53.0/0.3	10.3/35.9/63.4/0.7
Cu(7)Fe(3)-Si	1.8/66.6/28.7/4.7	3.4/56.5/38.8/4.7	6.0/46.5/49.0/4.5	10.0/35.7/57.8/6.5
Cu(10)-Si	0.1/64.8/35.2/0.0	0.2/52.2/47.2/0.6	0.4/41.8/57.5/0.7	0.9/29.7/69.5/0.8
Fe(10)-Si	0.9/29.1/52.9/18.0	1.6/25.4/54.5/20.1	2.7/22.5/55.6/21.9	4.6/18.0/54.6/27.4

As for the bi-metallic samples, the X_{CO_2} values in the range of 200–260 °C regularly rise from 1.8 to 11.6%, while the $S_{\text{CH}_3\text{OH}}$ decreases in the range 66.6–29.7%. Over these samples, the CH₄ selectivity also increases with temperature, at 260 °C resulting as low as 0.7% on Cu(5)Fe(5)-Si, while 6.5–7.0% on the other bi-metallic samples, values anyhow lower than that obtained under the same temperature over the mono-metallic copper-free sample (S_{CH_4} , 27.4%). However, these results confirm a poorer catalytic performance with respect to benchmark CZA or CZZ systems tested under similar conditions [26,27]; furthermore, they clearly put in evidence the beneficial cooperative effect between copper and iron atoms in driving the production of methanol via direct CO₂ hydrogenation. Yet, both the

metal loading and the iron fraction depict a determinant control on the activity-selectivity pattern, so that thorough data normalization is necessary for a full understanding of the catalytic behaviour. In this respect, by elaborating the rate of CO₂ conversion as a function of the number of oxygen vacancies, in turn determined from the CO₂ adsorbed on medium-strong sites, the “turnover frequency” over each catalyst sample was calculated and put in relation to the atomic iron fraction.

The bell-shaped curve shown in Figure 8 visibly evidences the need of an optimal relative concentration of iron atoms to maximize the rate of CO₂ conversion, indirectly disclosing how a large number of oxygen vacancies is necessary to favour the adsorption of carbon dioxide, but not sufficient to lower the energy barrier associated with the cleavage of C=O bonds and then to activate CO₂ under the adopted conditions.

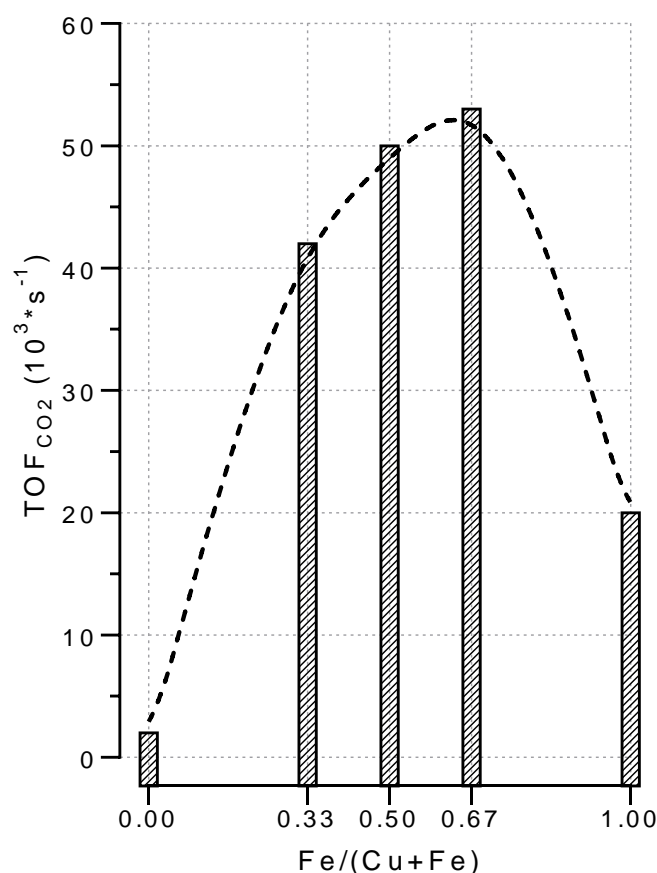


Figure 8. Turnover frequency of CO₂ conversion on oxygen vacancies. Experimental data calculated at 30 bar and 220 °C ($X_{\text{CO}_2} < 5\%$).

Despite the complexity in finding a basic relationship comprehensively describing the catalytic behaviour, it is, nevertheless, observable that the Cu(3)Fe(7)-Si sample characterized by a Fe/(Cu + Fe) ratio of 0.67 exhibits the highest turnover frequency of CO₂, suggesting that the CO₂ hydrogenation reaction over Cu(x)Fe(y)-Si catalysts takes advantage from the presence of a prevailing concentration of metallic Fe (see Figure 3—right), evidently acting as the active site for the primary formation of CO via rWGS [56]. Then, the CO adsorbed on metallic Fe can be further hydrogenated till methanol, likely owing to a phase change occurred in the Fe sites in the form of carbides as generated on the Fisher-Tropsch catalysts [57]. On the opposite site, the Cu-rich catalyst compositions, like in Cu(7)Fe(3)-Si, depress the kinetics of the rWGS route, rather addressing a formate pathway very common on Cu-based catalysts under CO₂-to-MeOH hydrogenation conditions [58]; the active site being essentially associable to the existence of a large metallic copper phase in strong interaction with a poorly reducible iron oxide phase. Still, on

catalysts characterized by an equimolar concentration of copper and iron sites, a “pure” specific mechanism (whether rWGS or formate route) is not really dominant, so that the extent of interaction between the copper oxide and the iron oxide phases requires a certain period for the complete sample reduction and the possible conversion of metallic Fe into carbides via rWGS. Indeed, the lowest selectivity to methane at 260 °C on the Cu(5)Fe(5)-Si sample (S_{CH_4} , 0.7%) is the result of the lack of a really “pure” mechanism, evidently due to the co-existence of mixed phases on the micro-spherical silica.

The catalytic stability evaluated in terms of CO₂ conversion as a function of time-on-stream is shown in Figure 9.

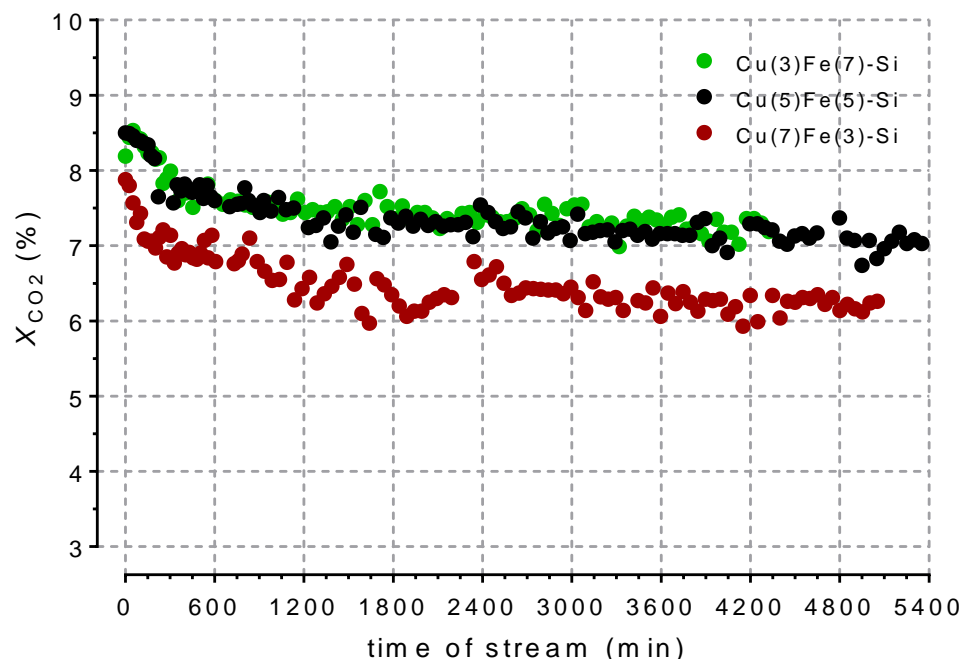


Figure 9. Trend of CO₂ conversion (X_{CO_2}) with time on stream. Reaction conditions: P_R , 30 bar; T_R , 260 °C; CO₂/H₂/N₂: 3/9/1; GHSV: 8800 NL/kg_{cat}/h; tos, 5400 min.

It can be observed that, irrespective of the differences in the absolute values recorded on the bi-metallic Cu(x)Fe(y)-Si catalysts, the activity pattern in all the cases reaches an almost steady state after about 600 min from the start of the experiments, then not showing any further decay for over 4500 min.

The “post reaction” analysis performed on the catalyst samples proves that no coke (see Figure S2 in the Supplementary Materials) or metal sintering (crystallite size almost unchanged with respect to the fresh sample) can be invoked to justify the observed loss of catalytic activity during the first phase of reaction, rather the presence of a peak reflection at 45° in the XRD pattern confirms the formation of an iron carbide phase (Fe₃C, JPCSD 06-0670) during reaction, envisaging a structural modification due to an incipient iron carburization (see Figure 10). Moreover, a clear signal centred at around 38° and associated with the generation of a spinel CuFe₂O₄ phase on Cu(5)Fe(5)-Si (not visible in the other “used” bi-metallic samples) clearly corroborates the insight into the existence of mixed phases on the micro-spherical silica support, being well known that a poorly reducible phase (i.e., spinel-like) leads to a lower surface coverage of adsorbed H species, so preventing the complete hydrogenation till methane [59].

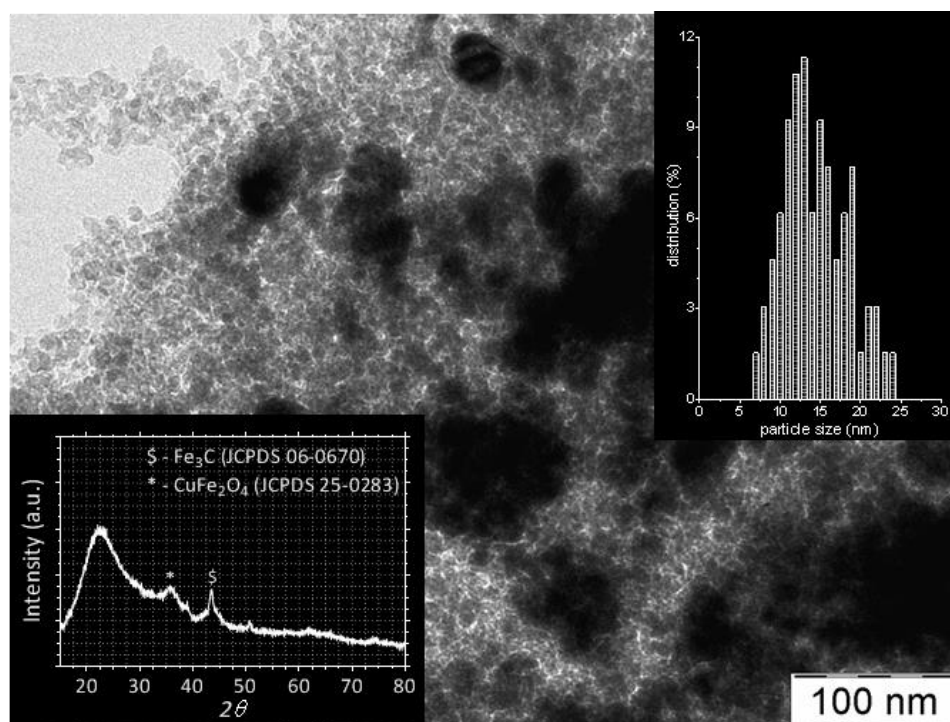


Figure 10. TEM image of the Cu(3)Fe(7)-Si sample after run (P_R , 30 bar; T_R , 260 °C; GHSV: 8800 NL/kg_{cat}/h; tos, 5400 min).

3. Materials and Methods

3.1. Catalyst Preparation

A commercial micro-spherical silica ES70Y (SA_{BET} : 295 m²/g; PV : 1.6 cm³/g) supplied by PQ Corporation was used as the support of bimetallic Cu(x)Fe(y)-SiO₂ catalytic samples. Cu(NO₃)₂·3H₂O and Fe(NO₃)₃·9H₂O (supplied by Sigma Aldrich) were together dissolved in a suitable amount of water, prior to being impregnated on the silica support, by changing the Cu:Fe atomic ratio from 2:1 to 1:2. Monometallic Cu/SiO₂ and Fe/SiO₂ catalysts were prepared by dry impregnation method starting from the aqueous solutions of the nitrate precursors. After impregnation, the catalysts were dried in air at 110 °C for 12 h and calcined in static air at 400 °C for 4 h.

3.2. Characterization

The analytical composition of catalysts was determined by X-ray fluorescence analysis, using a *Bruker AXS-S4 Explorer* spectrometer (Karlsruhe, Germany), equipped with a rhodium X-ray source (Rh anode and 75 μm Be window), a LiF 220 crystal analyzer and a 0.12° divergence collimator. Samples were analysed at the solid state, taking into account the emission value of Cu-Kα1 and Fe-Kα1 transitions.

The specific surface area and the pore volume data were obtained by elaboration of the nitrogen adsorption isotherm (−196 °C) according to the BET and BJH methods. The measurements were performed in a *Micromeritics ASAP 2020* instrument (Norcross, GA, USA), upon reduction in the samples in flowing H₂ at 400 °C, being then passivated at 25 °C in a 2% O₂/He flow.

The sample structure was analysed by a *Philips X-Pert diffractometer* (Amsterdam, The Netherlands), operating with a Ni β-filtered Cu Kα radiation ($\lambda = 1.5406 \text{ \AA}$) at 40 kV and 30 mA and a scan step of 0.05° s^{−1}.

The measurements of reducibility under hydrogen atmosphere (TPR) were performed in a customized micro-plant by using a linear quartz micro-reactor (*i.d.*, 4 mm) fed with a 5.6 vol.% H₂/Ar mixture at the flow rate of 60 STP mL/min. The experiments were carried out in the range 25–800 °C, with a heating rate of 12 °C/min. The hydrogen consumption

was monitored by a thermal conductivity detector, calibrated by the peak area of a known amount of CuO. TPR data resulted in being very reproducible both in terms of maximum position (± 3 °C) and extent of H₂ consumption ($\pm 3\%$).

TEM micro-graphs of the “fresh” and “used” hybrid catalysts were acquired and elaborated by a *Philips CM12* instrument equipped with a high-resolution camera. Powdered samples were dispersed in 2-propanol under ultrasound irradiation and the resulting suspension put drop-wise on a holey carbon-coated support grid.

SEM analysis was carried out to study the morphology of the prepared catalysts by using a *Philips XL-30-FEG* instrument (Eindhoven, The Netherlands). An EDAX analyzer (*Oxford, model 6587*) was used to determine the atomic composition, with specimens of catalyst samples deposited as powders on pin flat stubs.

Measurements of temperature-programmed desorption of carbon dioxide (CO₂-TPD) were performed in the experimental setup used for TPR to determine the surface concentrations of base sites. Before CO₂-TPD experiments, the catalyst samples (~100–200 mg) were reduced in a linear quartz micro-reactor (*l.*, 200 mm; *i.d.*, 4 mm) at atmospheric pressure, by flowing hydrogen (100 STP mL/min) from room temperature to 400 °C (heating rate of 10 °C/min). After an isothermal step of 60 min at 300 °C under hydrogen flow, followed by purging with helium, the samples were saturated in a gas mixture of 20 vol.% CO₂/He (flow rate of 50 STP mL/min) for 60 min. Then, the samples were cooled down to 100 °C in He flow until a constant baseline level was maintained. The desorption measurements were carried out in a range from 100 to 500 °C, at a heating rate of 10 °C/min, using helium as the carrier flow (50 STP mL/min). The CO₂ (*m/z*, 44) desorption process was monitored by a *Pfeiffer Vacuum, ThermoStar*[®] quadrupole mass spectrometer (Asslar, Germany) equipped with a heated (150 °C) fast-response inlet capillary system, quantitatively calibrated by known pulses of CO₂.

The chemical environment of oxygen species was determined by X-ray photoelectron spectroscopy, using a Physical Electronics (PHI) 5800-01 spectrometer. The samples were previously outgassed overnight and then reduced “in situ” at 400 °C in an environmental chamber prior to being entered by a fork into the analysis chamber. A monochromatic Al-K α X-ray source was used at a power of 350 W. Spectra were obtained with pass energies of 11.75 eV. The Ag 3d_{5/2} peak of an argentine foil was taken after 30 min of argon sputtering for checking the calibration of the binding energy (BE) scale. XPS data have been interpreted by using the online library of oxidation states implemented in the *PHI MULTIPAK 6.1* software and the PHI Handbook of X-ray photoelectron spectroscopy. The spectra have been deconvoluted by using a linear combination of three Gaussian-Lorentzian model functions, superimposed to a Shirley background, as exemplified by the overlapping of three oxygen species associated with oxygen lattice (O_L) at 532 eV, oxygen vacancies (O_V) at 534 eV and oxygen chemisorbed (O_C) at 535 eV, respectively, with FWHM less than 2 eV.

3.3. Testing

The catalytic measurements were carried out in a fixed bed stainless steel reactor (*i.d.*, 4 mm; *l.*, 200 mm) jacketed within a stainless steel rod (*o.d.*, 14 mm; *l.*, 180 mm) to maintain an effective control of temperature during the run. The catalytic data were achieved at 30 bar, in a range of temperature between 200 and 260 °C, with a feed mixture CO₂/H₂/N₂ at a volumetric ratio of 3/9/1, operated at a space velocity of 8800 NL/kg_{cat}/h. For each test, the 40–70 mesh fraction was chosen as a suitable compromise between the pressure drop along the reactor and the mechanical resistance of catalyst particle. All the catalysts were pre-reduced in situ at 400 °C for 1 h under a “pure” hydrogen flow at atmospheric pressure. The composition of the reaction stream was online, analysed by means of a gas chromatograph connected to the reactor outlet by means of two lines heated to 150 °C and equipped with two sampling valves and two injection systems connected to two detectors: TCD (thermoconductivity detector) and FID (flame ionization detector), for the analysis of permanent gases and carbon compounds (methane, methanol, ...), respectively. The separation systems consisted of a molecular sieve column in series with a

Porapak Q column for permanent gas analysis and a *HayeSep*[®] packed column for methanol and methane analysis.

In addition, the analytical system included the use of a shear column for water, with associated flow reversal. Chromatographic analysis was conducted under isothermal conditions at 80 °C. Both internal standard and mass-balance methods were adopted for the calculation of conversion-selectivity data, with an accuracy of $\pm 3\%$ and carbon balance close to 100%.

4. Conclusions

A silica sample, characterized by a uniform distribution of regular spheres, was used as support either for mono-metallic Cu and Fe samples or for bi-metallic Cu-Fe systems at variable Cu/Fe atomic ratio, finally allowing for the generation of a metallic phase with particle size between 13 and 19 nm.

TPR measurements emphasized how the Cu/Fe ratio controls the synergy between the metal oxides particles, significantly affecting the reduction kinetics in each sample. Two main CO₂ adsorption sites were identified by TPD measurements, corresponding to metal-oxygen pairs (weak-medium sites) and oxygen vacancies (medium-strong sites), respectively. A clear relationship between the CO₂ adsorption capacity and the relative concentration of oxygen vacancies highlighted that the adsorbed hydrogen can generate oxygen vacancies on the sample surface or induce their migration from inside the bulk oxide to the catalyst surface, as prompted on the systems where an Fe enrichment on the silica support was realized.

The catalytic activity measured at 30 bar in the temperature range 200–260 °C during the hydrogenation of CO₂ to methanol showed, for all the samples, a progressive increase in the CO₂ conversion with temperature, while methanol selectivity exhibited a clear drop, offset by a regular rise in CO and CH₄ selectivity. On the whole, the catalytic results put clearly in evidence the beneficial cooperative effect between copper and iron atoms in driving the production of methanol, the highest methanol yield of 4.1% being achieved on the Cu(3)Fe(7)-Si sample at a maximum CO₂ conversion of 11.6%. The rationalization of the catalytic disclosed how a large number of oxygen vacancies is a necessary but not sufficient condition to lower the energy barrier associated with the cleavage of C=O bonds and then to activate CO₂ under the adopted conditions. Anyhow, an optimal relative concentration of iron atoms resulted in being crucial for maximizing the rate of CO₂ conversion, addressing a specific mechanism of methanol formation via rWGS, contrarily to the formate route mainly suggested for Cu-based catalyst compositions under CO₂ hydrogenation conditions.

Without evidence for a catalytic deactivation, due to coke formation or metal sintering, the initial loss of activity during the stability test was put in relation to the formation of an iron carbide phase during reaction, mirroring an incipient surface reconstruction. The appearance of a spinel CuFe₂O₄ phase on the “used” Cu(5)Fe(5)-Si sample clearly demonstrated that the catalyst composition controls the formation of mixed phases (i.e., spinel-like), so determining a specific surface coverage of adsorbed H species and affecting the final product selectivity.

Supplementary Materials: The following supporting information can be downloaded at: <https://www.mdpi.com/article/10.3390/catal12060603/s1>, Figure S1: Cu2p XPS (a) and Fe2p XPS (b) spectra for the Cu(10)-Si and Fe(10)-Si samples respectively; Figure S2: TG-DSC analysis on the Cu(3)Fe(7)-Si sample after the stability test (PR, 30 bar; TR, 260 °C; GHSV: 8800 NL/kgcat/h; tos, 5400 min).

Author Contributions: Conceptualization, D.W.; methodology, I.M.-K. and G.B.; investigation, S.T., F.F. and C.C.; data curation, G.B.; writing—original draft preparation, S.T.; writing—review and editing, F.F. and G.B.; visualization, C.C.; supervision, D.W., J.-F.P.-R. and G.B.; project administration, G.B.; funding acquisition, D.W., J.-F.P.-R. and G.B. All authors have read and agreed to the published version of the manuscript.

Funding: This article has been supported by the Polish National Polish Agency for Academic Exchange (NAWA) through the BIOCO2 project (Grant no. PPI/APM/2019/1/00042/U/00001). The project leading to this submission received funding from the Italian Ministry for Education, University, and Research (MIUR) within the research program PRIN no. 2017WR2LRS.

Data Availability Statement: Not applicable.

Acknowledgments: The authors also acknowledge the Joint bilateral Agreement and the Executive Protocol 2021–2022 between the Centro de Investigación y de Estudios Avanzados del Instituto Politécnico Nacional (CINVESTAV, Mexico) and the National Research Council of Italy (CNR) for the support through the project “Carbon nanobeads as active components for the production of bio-methanol via reduction of CO₂”.

Conflicts of Interest: The authors declare no conflict of interest.

References

1. Yoro, K.O.; Daramola, M.O. *Advances in Carbon Capture*; Rahimpour, M.R., Farsi, M., Makarem, M.A., Eds.; Woodhead Publishing: Cambridge, UK, 2020; pp. 3–28.
2. Kenarsari, S.D.; Yang, D.; Jiang, G.; Zhang, S.; Wang, J.; Russell, A.G.; Wei, Q.; Fan, M. Review of recent advances in carbon dioxide separation and capture. *RSC Adv.* **2013**, *3*, 22739–22773. [[CrossRef](#)]
3. Fawzy, S.; Osman, A.I.; Doran, J.; Rooney, D.W. Strategies for mitigation of climate change: A review. *Environ. Chem. Lett.* **2020**, *18*, 2069–2094. [[CrossRef](#)]
4. Meylan, F.D.; Moreau, V.; Erkman, S. CO₂ utilization in the perspective of industrial ecology, an overview. *J. CO₂ Util.* **2015**, *12*, 101–108. [[CrossRef](#)]
5. Zhang, Z.; Wang, T.; Blunt, M.J.; Anthony, E.J.; Park, A.A.; Hughes, R.W.; Webley, P.A.; Yan, J. Advances in carbon capture, utilization and storage. *Appl. Energy* **2020**, *278*, 115627–115680. [[CrossRef](#)]
6. Nocito, F.; Dibenedetto, A. Atmospheric CO₂ mitigation technologies: Carbon capture utilization and storage. *Curr. Opin. Green Sustain. Chem.* **2020**, *21*, 34–43. [[CrossRef](#)]
7. Markewitz, P.; Kuckshinrichs, W.; Leitner, W.; Linssen, J.; Zapp, P.; Bongartz, R.; Schreiber, A.; Müller, T. Worldwide innovations in the development of carbon capture technologies and the utilization of CO₂. *Energy Environ. Sci.* **2012**, *5*, 7281–7305. [[CrossRef](#)]
8. Soltanieh, M.; Mahmoodi Azar, K.; Saber, M. Development of a zero emission integrated system for co-production of electricity and methanol through renewable hydrogen and CO₂ capture. *Int. J. Greenh.* **2012**, *7*, 145–152. [[CrossRef](#)]
9. Hos, T.; Landau, M.V.; Herskowitz, M. Hydrogenation of CO₂ on Fe-Based Catalysts: Preferred Route to Renewable Liquid Fuels. *Eng. Chem. Res.* **2022**, *in press*. [[CrossRef](#)]
10. Matzen, M.; Demirel, Y. Methanol and dimethyl ether from renewable hydrogen and carbon dioxide: Alternative fuels production and life-cycle assessment. *J. Clean. Prod.* **2016**, *139*, 1068–1077. [[CrossRef](#)]
11. Catizzone, E.; Freda, C.; Braccio, G.; Frusteri, F.; Bonura, G. Dimethyl ether as circular hydrogen carrier: Catalytic aspects of hydrogenation/dehydrogenation steps. *J. Energy Chem.* **2021**, *58*, 55–77. [[CrossRef](#)]
12. Atspha, T.A.; Yoon, T.; Seongho, P.; Lee, C.J. A review on the catalytic conversion of CO₂ using H₂ for synthesis of CO, methanol, and hydrocarbons. *J. CO₂ Util.* **2021**, *44*, 101413–101435. [[CrossRef](#)]
13. Wang, J.; Zhang, G.; Zhu, J.; Zhang, X.; Ding, F.; Zhang, A.; Guo, X.; Song, C. CO₂ Hydrogenation to Methanol over In₂O₃-Based Catalysts: From Mechanism to Catalyst Development. *ACS Catal.* **2021**, *11*, 1406–1423. [[CrossRef](#)]
14. Schorn, F.; Breuer, J.L.; Samsun, R.C.; Schnorbus, T.; Heuser, B.; Peters, R.; Stolten, D. Methanol as a renewable energy carrier: An assessment of production and transportation costs for selected global locations. *Adv. Appl. Energy* **2021**, *3*, 100050–100064. [[CrossRef](#)]
15. Dalena, F.; Senatore, A.; Basile, M.; Knani, S.; Basile, A.; Iulianelli, A. Advances in Methanol Production and Utilization, with Particular Emphasis toward Hydrogen Generation via Membrane Reactor Technology. *Membranes* **2018**, *8*, 98. [[CrossRef](#)] [[PubMed](#)]
16. Müller, K.; Fabisch, F.; Artl, W. Energy Transport and Storage using Methanol as a Carrier. *Green* **2014**, *4*, 19–25. [[CrossRef](#)]
17. Meunier, N.; Chauvy, R.; Mouhoubi, S.; Thomas, D.; De Weireld, G. Alternative production of methanol from industrial CO₂. *Renew. Energy* **2020**, *146*, 1192–1203. [[CrossRef](#)]
18. Marlin, D.S.; Sarron, E.; Sigurbjörnsson, O. Process Advantages of Direct CO₂ to Methanol Synthesis. *Front. Chem.* **2018**, *6*, 446–454. [[CrossRef](#)]
19. Pérez-Fortes, M.; Schöneberger, J.C.; Boulamanti, A.; Tzimas, E. Methanol synthesis using captured CO₂ as raw material: Techno-economic and environmental assessment. *Appl. Energy* **2016**, *161*, 718–732. [[CrossRef](#)]
20. Bowker, M. Methanol Synthesis from CO₂ Hydrogenation. *ChemCatChem* **2019**, *11*, 4238–4246. [[CrossRef](#)]
21. Chauvy, R.; De Weireld, G. CO₂ Utilization Technologies in Europe: A Short Review. *Energy Technol.* **2020**, *8*, 2000627–2000644. [[CrossRef](#)]
22. Guil-López, R.; Mota, N.; Llorente, J.; Millán, E.; Pawelec, B.; Fierro, J.L.G.; Navarro, R.M. Methanol Synthesis from CO₂: A Review of the Latest Developments in Heterogeneous Catalysis. *Materials* **2019**, *12*, 3902. [[CrossRef](#)] [[PubMed](#)]
23. Kleiber, S.; Pallua, M.; Siebenhofer, M.; Lux, S. Catalytic Hydrogenation of CO₂ to Methanol over Cu/MgO Catalysts in a Semi-Continuous Reactor. *Energies* **2021**, *14*, 4319. [[CrossRef](#)]

24. Wu, Q.; Liang, S.; Zhang, T.; Louis, B.; Wang, Q. Hydrogen-rich syngas production from biomass pyrolysis and catalytic reforming using biochar-based catalysts. *Fuel* **2022**, *313*, 123006–123016. [[CrossRef](#)]
25. Leonzio, G.; Zondervan, E.; Foscolo, P.U. Methanol production by CO₂ hydrogenation: Analysis and simulation of reactor performance. *Int. J. Hydrog. Energy* **2019**, *44*, 7915–7933. [[CrossRef](#)]
26. Kanuri, S.; Roy, S.; Chakraborty, C.; Datta, S.P.; Singh, S.A.; Dinda, S. An insight of CO₂ hydrogenation to methanol synthesis: Thermodynamics, catalysts, operating parameters, and reaction mechanism. *Int. J. Energy Res.* **2022**, *4*, 5503–5522. [[CrossRef](#)]
27. Arena, F.; Barbera, K.; Italiano, G.; Bonura, G.; Spadaro, L.; Frusteri, F. Synthesis, characterization and activity pattern of Cu–ZnO/ZrO₂ catalysts in the hydrogenation of carbon dioxide to methanol. *J. Catal.* **2007**, *249*, 185–194. [[CrossRef](#)]
28. Arena, F.; Italiano, G.; Barbera, K.; Bordiga, S.; Bonura, G.; Spadaro, L.; Frusteri, F. Solid-state interactions, adsorption sites and functionality of Cu–ZnO/ZrO₂ catalysts in the CO₂ hydrogenation to CH₃OH. *Appl. Catal. A Gen.* **2008**, *350*, 16–23. [[CrossRef](#)]
29. Bonura, G.; Cordaro, M.; Cannilla, C.; Arena, F.; Frusteri, F. The changing nature of the active site of Cu–Zn–Zr catalysts for the CO₂ hydrogenation reaction to methanol. *Appl. Catal. B Environ.* **2014**, *152*, 152–161. [[CrossRef](#)]
30. Ding, M.; Qiu, M.; Wang, T.; Ma, L.; Wu, C.; Liu, J. Effect of iron promoter on structure and performance of CuMnZnO catalyst for higher alcohols synthesis. *Appl. Energy* **2012**, *97*, 543–547. [[CrossRef](#)]
31. Guo, H.; Zhang, H.; Peng, F.; Yang, H.; Xiong, L.; Wang, C.; Huang, C.; Chen, X.; Ma, L. Effects of Cu/Fe ratio on structure and performance of attapulgite supported CuFeCo-based catalyst for mixed alcohols synthesis from syngas. *Appl. Catal. A Gen.* **2015**, *503*, 51–61. [[CrossRef](#)]
32. Xu, D.; Ding, M.; Hong, X.; Liu, G.; Tsang, S.C.E. Selective C₂₊ Alcohol Synthesis from Direct CO₂ Hydrogenation over a Cs-Promoted Cu–Fe–Zn Catalyst. *ACS Catal.* **2020**, *10*, 5250–5260. [[CrossRef](#)]
33. Chen, C.-S.; Cheng, W.-H.; Lin, S.-S. Study of iron-promoted Cu/SiO₂ catalyst on high temperature reverse water gas shift reaction. *Appl. Catal. A Gen.* **2004**, *257*, 97–106. [[CrossRef](#)]
34. Xiao, K.; Bao, Z.; Qi, X.; Wang, X.; Zhong, L.; Lin, M.; Fang, K.; Sun, Y. Unsupported CuFe bimetallic nanoparticles for higher alcohol synthesis via syngas. *Catal. Commun.* **2013**, *40*, 154–157. [[CrossRef](#)]
35. Lu, Y.; Yu, F.; Hu, J.; Liu, J. Catalytic conversion of syngas to mixed alcohols over Zn–Mn promoted Cu–Fe based catalyst. *Appl. Catal. A Gen.* **2012**, *429*, 48–58. [[CrossRef](#)]
36. Gao, W.; Zhao, Y.; Liu, J.; Huang, Q.; He, S.; Li, C.; Zhao, J.; Wei, M. Catalytic conversion of syngas to mixed alcohols over CuFe-based catalysts derived from layered double hydroxides. *Catal. Sci. Technol.* **2013**, *3*, 1324–1332. [[CrossRef](#)]
37. Strekalova, A.A.; Shesterkina, A.A.; Kustov, L.M. Recent progress in hydrogenation of esters on heterogeneous bimetallic catalysts. *Catal. Sci. Technol.* **2021**, *22*, 7229–7238. [[CrossRef](#)]
38. Chen, K.; Yu, J.; Liu, B.; Si, C.; Ban, H.; Cai, W.; Li, C.; Li, Z.; Fujimoto, K. Simple strategy synthesizing stable CuZnO/SiO₂ methanol synthesis catalyst. *J. Catal.* **2019**, *372*, 163–173. [[CrossRef](#)]
39. Yang, H.; Gao, P.; Zhang, C.; Zhong, L.; Li, X.; Wang, S.; Wang, H.; Wei, W.; Sun, Y. Core–shell structured Cu@m-SiO₂ and Cu/ZnO@m-SiO₂ catalysts for methanol synthesis from CO₂ hydrogenation. *Catal. Commun.* **2016**, *84*, 56–60. [[CrossRef](#)]
40. Ren, S.; Shoemaker, W.R.; Wang, X.; Shang, Z.; Klinghoffer, N.; Li, S.; Yu, M.; He, X.; White, T.A.; Liang, X. Effects of mixing methods of bifunctional catalysts on catalyst stability of DME synthesis via CO₂ hydrogenation. *Fuel* **2019**, *239*, 1125–1133. [[CrossRef](#)]
41. Kattel, S.; Ramirez, P.J.; Chen, J.G.; Rodriguez, J.A.; Liu, P. Active sites for CO₂ hydrogenation to methanol on Cu/ZnO catalysts. *Science* **2017**, *355*, 1296–1299. [[CrossRef](#)]
42. Cui, X.; Yan, W.; Yang, H.; Shi, Y.; Xue, Y.; Zhang, H.; Niu, Y.; Fan, W.; Deng, T. Preserving the Active Cu–ZnO Interface for Selective Hydrogenation of CO₂ to Dimethyl Ether and Methanol. *ACS Sustain. Chem. Eng.* **2021**, *9*, 2661–2672. [[CrossRef](#)]
43. Lam, E.; Corral-Pérez, J.J.; Larmier, K.; Noh, G.; Wolf, P.; Comas-Vives, A.; Urakawa, A.; Copéret, C. CO₂ Hydrogenation on Cu/Al₂O₃: Role of the Metal/Support Interface in Driving Activity and Selectivity of a Bifunctional Catalyst. *Angew. Chem. Int. Ed.* **2019**, *58*, 13989–13996. [[CrossRef](#)]
44. Frusteri, L.; Cannilla, C.; Todaro, S.; Frusteri, F.; Bonura, G. Tailoring of Hydrotalcite-Derived Cu-Based Catalysts for CO₂ Hydrogenation to Methanol. *Catalysts* **2019**, *9*, 1058. [[CrossRef](#)]
45. Carvalho, D.F.; Almeida, G.C.; Monteiro, R.S.; Mota, C.J.A. Selective Hydrogenation of CO₂ to Hydrocarbons: Effects of Fe₃O₄ Particle Size on Reduction, Carburization, and Catalytic Performance. *Energy Fuels* **2020**, *34*, 7269–7274. [[CrossRef](#)]
46. Dasireddy, V.D.B.C.; Likozar, B. The role of copper oxidation state in Cu/ZnO/Al₂O₃ catalysts in CO₂ hydrogenation and methanol productivity. *Renew. Energy* **2019**, *140*, 452–460. [[CrossRef](#)]
47. Bonura, G.; Cannilla, C.; Frusteri, L.; Catizzzone, E.; Todaro, S.; Migliori, M.; Giordano, G.; Frusteri, F. Interaction effects between CuO–ZnO–ZrO₂ methanol phase and zeolite surface affecting stability of hybrid systems during one-step CO₂ hydrogenation to DME. *Catal. Today* **2020**, *345*, 175–182. [[CrossRef](#)]
48. Witoon, T.; Chalorngham, J.; Dumrongbunditkul, P.; Chareonpanich, M.; Limtrakul, J. CO₂ hydrogenation to methanol over Cu/ZrO₂ catalysts: Effects of zirconia phases. *Chem. Eng. J.* **2016**, *293*, 327–336. [[CrossRef](#)]
49. Faungnawakij, K.; Kikuchi, R.; Fukunaga, T.; Eguchi, K. Catalytic hydrogen production from dimethyl ether over CuFe₂O₄ spinel-based composites: Hydrogen reduction and metal dopant effects. *Catal. Today* **2008**, *138*, 157–161. [[CrossRef](#)]
50. Messi, C.; Carniti, P.; Gervasini, A. Kinetics of reduction of supported nanoparticles of iron oxide. *J. Therm. Anal. Calorim.* **2008**, *91*, 93–100. [[CrossRef](#)]
51. Etim, U.J.; Zhang, C.; Zhong, Z. Impacts of the Catalyst Structures on CO₂ Activation on Catalyst Surfaces. *Nanomaterials* **2021**, *11*, 3265. [[CrossRef](#)]

52. Li, K.; Chen, J.C. CO₂ Hydrogenation to Methanol over ZrO₂-Containing Catalysts: Insights into ZrO₂ Induced Synergy. *ACS Catal.* **2019**, *9*, 7840–7861. [[CrossRef](#)]
53. Guo, J.; Luo, Z.; Hu, G.T.; Wang, Z. Synthesis of oxygen vacancies enriched Cu/ZnO/CeO₂ for CO₂ hydrogenation to methanol. *Greenh. Gas. Sci. Technol.* **2021**, *11*, 1171–1179. [[CrossRef](#)]
54. Mora, J.C.; Nederstigt, Y.C.M.; Hill, J.M.; Ponnurangam, S. Promoting Effect of Supports with Oxygen Vacancies as Extrinsic Defects on the Reduction of Iron Oxide. *J. Phys. Chem. C* **2021**, *125*, 14299–14310. [[CrossRef](#)]
55. Zhu, M.; Tian, P.; Kurtz, R.; Lunkenbein, T.; Xu, J.; Schlögl, R.; Wachs, I.E.; Han, Y.-F. Strong Metal–Support Interactions between Copper and Iron Oxide during the High-Temperature Water-Gas Shift Reaction. *Angew. Chem. Int. Ed.* **2019**, *58*, 9083–9087. [[CrossRef](#)]
56. Numpilai, T.; Witoon, T.; Chanlek, N.; Limphirat, W.; Bonura, G.; Chareonpanich, M.; Limtrakul, J. Structure–activity relationships of Fe-Co/K-Al₂O₃ catalysts calcined at different temperatures for CO₂ hydrogenation to light olefins. *Appl. Catal. A Gen.* **2017**, *547*, 219–229. [[CrossRef](#)]
57. Wezendonk, T.A.; Sun, X.; Dugulan, A.I.; van Hoof, A.J.F.; Hensen, E.J.M.; Kapteijn, F.; Gascon, J. Controlled formation of iron carbides and their performance in Fischer-Tropsch synthesis. *J. Catal.* **2018**, *362*, 106–117. [[CrossRef](#)]
58. Bonura, G.; Todaro, S.; Frusteri, L.; Majchrzak-Kuceba, I.; Wawrzyńczak, D.; Pászti, Z.; Tálas, E.; Tompos, A.; Ferenc, L.; Solt, H.; et al. Inside the reaction mechanism of direct CO₂ conversion to DME over zeolite-based hybrid catalysts. *Appl. Catal. B Environ.* **2021**, *294*, 120255–120264. [[CrossRef](#)]
59. Kameoka, S.; Tanabe, T.; Tsai, A.P. Spinel CuFe₂O₄: A precursor for copper catalyst with high thermal stability and activity. *Catal. Lett.* **2005**, *100*, 89–93. [[CrossRef](#)]